Global and Planetary Change 169 (2018) 202–213

Contents lists available at ScienceDirect

Global and Planetary Change

journal homepage: www.elsevier.com/locate/gloplacha

Research article

Estimation of surface flow speed and ice surface temperature from optical satellite imagery at Viedma glacier, Argentina

Lo Vecchio A.[a,b,*], Lenzano M.G.[a], Durand M.[a], Lannutti E.[a], Bruce R.[a], Lenzano L.[a,b]

[a] Instituto argentino de Nivología, Glaciología y Ciencias Ambientales, CONICET-MENDOZA, Av. Ruiz Leal S/N Parque General San Martín, Ciudad de Mendoza, Argentina

[b] Estudios del Ambiente y Recursos Naturales, Departamento de Geografía, Facultad de Filosofía y Letras, Universidad Nacional de Cuyo, Argentina

A B S T R A C T

The Viedma glacier is the largest glacier in Argentina and one of the most dynamic in the Southern Patagonian Icefield. It is a strategic water source. This study analyzes the interactions of glaciological variables that help better explain the behavior of the Viedma glacier. This paper presents the study of surface flow speed and ice surface temperatures during the 2015–2016 warm season by using remote sensing data and includes the statistical correlation between those variables. In addition, a reconstruction of the front fluctuation between 1979 and 2016 through CORONA and LANDSAT images is included. Finally, the displacement modes dominating the Viedma glacier are suggested. Our results showed that the mean surface flow speed during the study period was of around 1.2 ± 0.3 md^{-1} and reached maximum values of 5.5 ± 0.3 md^{-1} and 3 ± 0.3 md^{-1} at middle basin and terminus respectively. Thermal data revealed minimum values of −2 °C in the uppermost section of the study area, whilst the glacier's terminus showed supraglacial melt (values above pressure melting point). Front fluctuation analysis revealed the largest front retraction of the last 40 years between 2010 and 2016: around 281 my^{-1}. Statistical correlation analysis and glaciological data suggested that the middle and lower basins of the Viedma glacier are widely dominated by basal sliding.

1. Introduction

Over the last 150 years, the globally accelerating rate of glacier retreat has been widely recognized (Solomina et al., 2016) and this is equally apparent in the Southern Patagonian Ice Field (SPI). The SPI is one of the world's largest ice masses (Pfeffer et al., 2014), and is located in the Austral Andes mountain range, between 48°30′S and 51°50′S, along the volcanic arc termed Austral Volcanic Zone (Stern et al., 1984). The SPI hosts large masses of temperate ice (Skvarca et al., 2002) and according to Mouginot and Rignot (2015), various SPI outlet glaciers are among the fastest moving in the world, except for some cases observed in Greenland. Several works have showed strong evidence of SPI glaciers retreat (Aniya and Skvarca, 1992; Naruse and Aniya, 1992; Rivera et al., 2008; Chen et al., 2007; Ivins et al., 2011; Rivera et al., 2012; Willis et al., 2012, Davies and Glasser, 2012; Mouginot and Rignot, 2015 and Moragues et al., 2018). In this sense, according to Liboutry (1956), Naruse and Aniya (1992), Aniya et al. (1996) and Arendt et al. (2012), the SPI lost 1200 km^2 between 1944 and 2012, which represents around 8.8% of the total area in 1944, around 13,500 km^2 (Liboutry, 1956).

Surface flow speed is a great indicator of glacier dynamics. Glacier flow transfers ice from high elevation accumulation areas to areas where ice is lost by melting and calving, and hence plays a major role in the hydrological cycle (Benn and Evans, 2014). In temperate glaciers, surface flow speed (Us) is defined by: *internal ice deformation* or *ice creep* (Ui) and *basal sliding* (Ub) (Benn and Evans, 2014) (Eq. (1)):

$$Us = Ub + Ui \quad (1)$$

where *Us* is surface flow speed, *Ub* is flow speed by basal sliding and *Ui* is flow speed by ice deformation.

Also, glacier terminus surface flow speed may be modified by the *calving effect* (Ce). Therefore, a temperate glacier commonly exhibits intra-annual flow speed variations depending on the dominant displacement mechanism at that time (Willis, 1995): **Ui)** According to Glen's flow laws, displacement due to internal ice deformation is closely related to ice temperature (Paterson, 1969), so that ice deforms much more readily as it warms toward its pressure melting point (Benn and Evans, 2014). **Ub)** The ice temperature increase may raise the melting rate and provide a higher melt water flow to the englacial and subglacial systems. In this sense, water plays an important role in the regelation process and in modulating frictional drag (Bennett and Glasser, 2011). **Ce)** Calving is a glacial ablation process that causes the greatest mass loss from the ice shelves of Antarctic, Greenland, and numerous glaciers in Alaska, Patagonia and other regions (Benn and Evans, 2014). Surface flow speed at glacier terminus may increase due to a reduction of basal drag and effective pressure, which are significantly affected by

* Corresponding author at: Instituto argentino de Nivología, Glaciología y Ciencias Ambientales, CONICET-MENDOZA, Av. Ruiz Leal S/N Parque General San Martín, Ciudad de Mendoza, Argentina.

E-mail address: anlovecchio@mendoza-conicet.gob.ar (A. Lo Vecchio).

https://doi.org/10.1016/j.gloplacha.2018.08.001
Received 3 May 2017; Received in revised form 26 July 2018; Accepted 1 August 2018
Available online 02 August 2018
0921-8181/

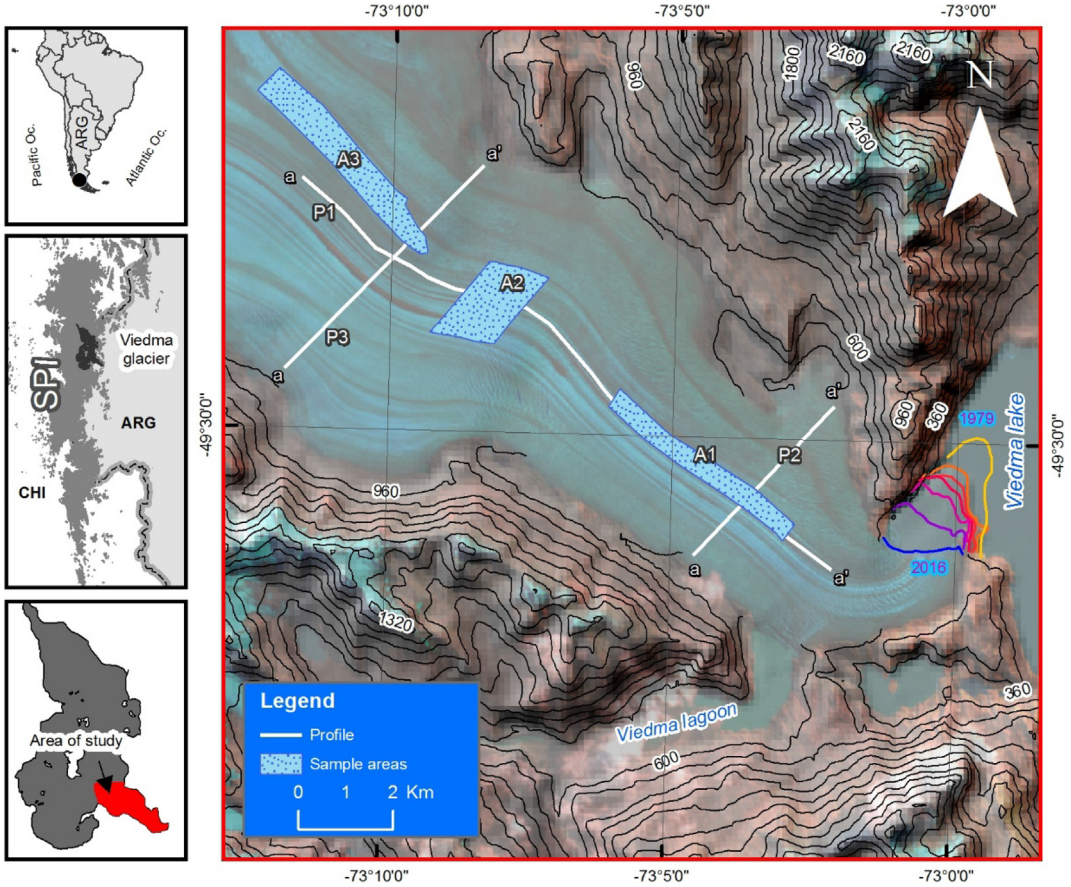

Fig. 1. The left panels indicate the study area. On the right panel, P1, P2 and P3 show the profiles used in velocities and surface temperatures analysis. The light blue background polygons (A1, A2 and A3) denote the sampling areas for the correlation analysis.

the presence of water at the margin, especially if it is deep enough for the ice to float fully or partially (Cuffey and Paterson, 2010).

Although the Viedma glacier (VG) is one of the largest and fastest SPI calving and temperate outlet glaciers (with an area of 963km^{2}in March 2016) (Fig. 1),few data have been collected regarding the VG's surface flow speed and its seasonal changes (Jaber et al., 2012; Riveros et al., 2013; Sakakibara and Sugiyama, 2014; Euillades et al., 2016; and Lenzano et al., 2018) and front fluctuation (Lopez et al., 2010; Sakakibara and Sugiyama, 2014). We have not found any studies on displacement modes at the VG. According to the surface flow speed results shown by Jaber et al. (2012), Euillades et al. (2016) and Lenzano et al. (2018), there is consensus that the mean surface flow speed at the VG's terminus is between 3 md^{-1} and 2 md^{-1} at middle basin. With respect to front fluctuation and the calving rate, Lopez et al. (2010) showed that the VG retreated < 1 km during the 1945–2005 period (60 years) with a mean rate of around 16 my^{-1}), and, later, Sakakibara and Sugiyama (2014) reported that the VG's front retreated at mean rates of 35.5 my^{-1}from 1984 to 2011 (27 years).

Regarding displacement mechanisms or modes, there is a general lack of knowledge about the SPI that includes the Viedma glacier as well. However, Stuefer et al. (2007) found that, at the terminus zone of the Perito Moreno glacier, basal sliding represented around 90% of the surface velocities. Recently, Mouginot and Rignot (2015) concluded that large portions of the SPI must be sliding over their beds. Meanwhile, Sugiyama et al. (2016) observed the high influence of basal water pressure on flow speed changes.

Advances in space technology have facilitated the use of satellite data to study complex physical processes in the glaciology field (Raj and Fleming, 2008).Thus, taking into account the immensity and the unaffordable nature of glacial environments, remote sensing may be the only effective tool to study glaciers comprehensively (Shukla et al., 2010), and the most practical way to obtain a continuous spatial measurement (Whillans and Tseng, 1995; Möller et al., 2007; Bown et al., 2008; Hall et al., 2008; Berthier et al., 2016, among others).

Therefore, the goal of this study is to provide **i)** the accurate surface flow speed (Us) and Ice Surface Temperature (IST) of the Viedma glacier in the warm season through remote sensing geospatial data from October 2015 to March 2016; and **ii)**the first approach to assess the relationship between Us and IST by remote sensing. In both cases, we compared the data at the beginning and at the end of the warm season to obtain the intra-seasonal changes and to address also the displacement modes. For the calculation of Us and IST we used LANDSAT 8 images. In order to estimate Us, we used the CIAS module, developed first by Kääb and Vollmer (2000), and later by Heid and Kääb (2012). In order to estimate IST, we used thermal infrared bands in conjunction with atmospheric and emissivity corrections (Barsi et al., 2003, 2005). This study aims at contributing to a better understanding of the Viedma glacier dynamics and the interactions among its physical processes.

2. Data and methods

The overall processing workflow is shown in Fig. 2. During the processing, the surface flow speed (Section 2.1) and the Ice surface temperature (Section 2.2) were calculated by means of 4 LANDSAT8 imageries. Images were chosen on the basis of free cloud cover and seasonal snow, which significantly reduces the number of available images (Table 1). Two pairs of images were selected with temporal proximity, corresponding to the beginning and the end of the 2015–2016 warm season in these latitudes. The 2015 pair covers from Oct.13, −2015 to Oct.29, 2015, and the 2016 pair covers from Feb.18,-

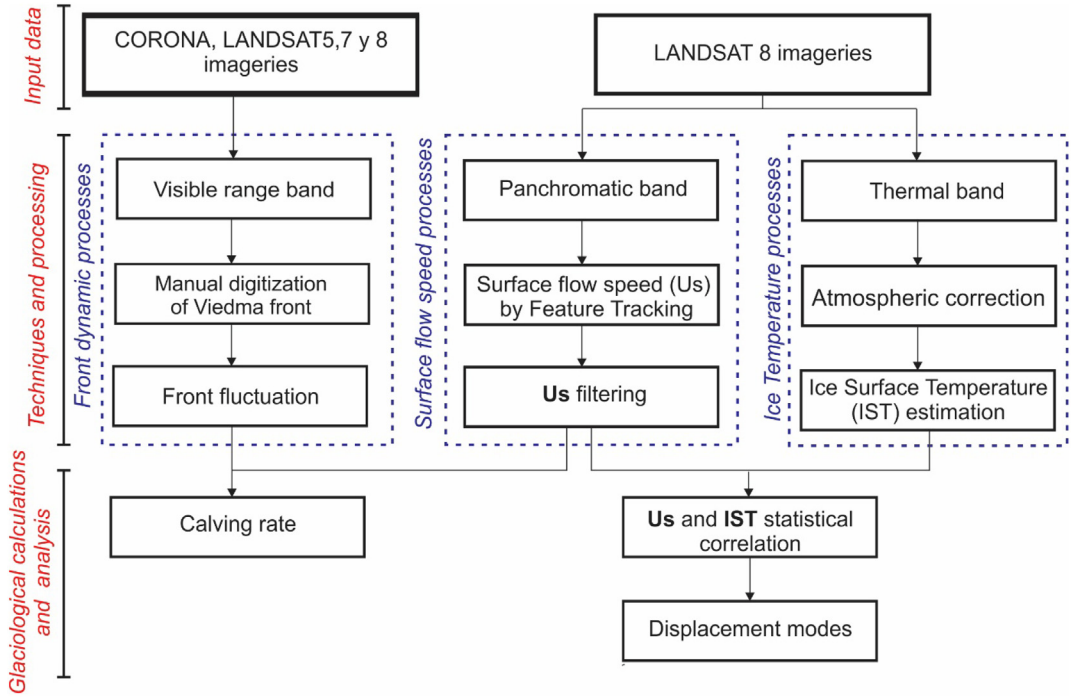

Fig. 2. Workflow of the study.

2016 to March-21,-2016. Finally, front fluctuations between 1979 and 2016 were estimated by means of 18 CORONA and LANDSAT 5, 7, 8 imageries.

From the surface flow speed and front fluctuation results, we estimated the Viedma glacier's calving rate from Oct. 13, 2015 to March 21, 2016 (Section 2.3). Later, the correlation between surface flow speed and ice surface temperature allowed us to obtain the displacement modes of the Viedma glacier (Section 2.4). Spatial data integration was made in Quantum GIS 2.14. The comparative analysis between the 2015 and 2016 pairs (both Us and IST) was made pixel by pixel for the whole study area, and, at some relevant places, through 3 profiles (P1 – at central Flow line-; P2 and P3, transversal profile) (see Fig. 1).

2.1. Surface flow speed (Us) by remote sensing

In order to obtain the vectors field of surface flow speed through the CIAS module (Image Correlation Software), a series of pre-process steps were followed. These included co-registration, orthorectification by using the 3D Model Shuttle Radar Topography Mission -SRTM- (https://lta.cr.usgs.gov/SRTM1Arc), and high pass filter application to highlight edges and boundaries (Berthier et al., 2003; Kumari et al., 2014). The CIAS module uses feature tracking technique through Normalized Cross-Correlation algorithm (Kääb and Vollmer, 2000; Heid and Kääb, 2012).The feature tracking technique requires the selection of pixels conjunct (Reference block) at master image to subsequently identify the same region at the slave image (Scambos et al., 1992). To this end, we determined the reference block (equal to 15 pixels for both pairs). Then, we determined the search area size (equal to 8 and 12 for the 2015 and 2016 pairs respectively) defined by the time lapse between the captures of the images making up the pair (Berthier et al., 2003; Kääb and Leprince, 2014).

Afterwards, the CIAS results were post-processed by means of filters applied to discard data with a low degree of cross-correlation confidence and incoherent flow direction vectors according to their context (Scherler et al., 2008; Kääb and Leprince, 2014). Thus, the filtering sequence started by **a)** discarding the data that showed coefficients of maximum correlation lower than 0.7, and, subsequently, **b)**the directional filter discarded data that presented an opposite direction to the glaciers' general flow.

2.1.1. Error evaluation

Feature tracking produces systematic and random errors, caused by the images co-registration and cross-correlation respectively (Berthier et al., 2003). Systematic error was estimated from the standard deviations (σ) obtained from the co-registration and the temporal time between the images of the pairs used (Δt) according to Eq. (2):

Table 1
LANDSAT 8 images and atmospherics parameters used in this work to Feature tracking technique. Ld is Downward radiance, Lu is Upward radiance and t is transmissivity. Both Ld and Lu are expressed in W/m2/sr/um.

Pair	ID	Band	Resolution (m)	Date	Acquisition time (Z)	Atmospherics parameters by NCEP		
						Ld	Lu	t
2015	LC82310952015286LGN00	Panchromatic	15	10/13/2015	14:26	0.91	0.53	0.91
		Thermal(b10)	100					
	LC82310952015302LGN00	Panchromatic	15	10/29/2015	14:26	0.50	0.29	0.95
		Thermal(b10)	100					
2016	LC82310942016049LGN00	Panchromatic	15	02/18/2016	14:25	0.80	0.47	0.92
		Thermal(b10)	100					
	LC82310942016081LGN00	Panchromatic	15	03/21/2016	14:25	1.45	0.87	0.86
		Thermal(b10)	100					

$$\sigma_{sist} = \sigma/\Delta t \ [md^{-1}] \quad (2)$$

Meanwhile, the random error can be considered as a white noise (Gaussian) in the shifting (displacements), where the noise of the components x and y of the correlation are considered as random independent variables and have normal distribution with variance σ^2. The modules respond to Raleigh's distribution and have a media $\mu = \sigma\sqrt{\pi/2}$ (Meikle, 2008; Herman et al., 2011). In this study, x and y correspond to the displacements observed over stable areas such as rock outcrops, and μ can be estimated through the Euclidean norm. Then, total error (σ_{total}) is defined by Eq. (3) (Berthier et al., 2003):

$$\sigma_{total} = \sqrt{\sigma_{sist}^2 + \sigma_{rand}^2} \quad (3)$$

2.2. Ice Surface Temperatures (IST) by remote sensing

The Thermal Infrared Sensor (TIRS) on LANDSAT 5, 7 and 8 can measure IST through Planck's function (Chuvieco, 2007). The TIRS uses Quantum Well Infrared Photodetectors (QWIPs) to detect long wavelengths of light emitted by the Earth, whose intensity depends on surface temperature. These wavelengths, called thermal infrared, are far from the range of human vision (NASA, 2017). In order to adjust the top-of-atmosphere (TOA) brightness temperature to a surface skin temperature, from the single TIR band, a separate atmospheric correction must be done, and the target emissivity must be prescribed. According to Barsi et al. (2003), IST can be estimated with an error of ± 2 Celsius degrees (°C) when the emissivity is known, and the atmosphere conditions are relatively clear.

One way to assess the accuracy of remotely-sensed IST is to compare the values with in-situ IST. There are many factors that complicate the task such as the fact that in-situ observations are point measurements while the satellite-derived observations represent IST from a much larger area (Hall et al., 2008). Throughout the SPI, the number of weather stations is low and not significant (Garreaud, 2009; Garreaud et al., 2014). Furthermore, in-situ observation from these stations is generally obtained at some height above the surface so that the measured air temperature is extrapolated to a surface temperature (Hall et al., 2008, 2012 and Hall et al., 2013).

2.2.1. Atmospheric and emissivity corrections

Atmosphere distortions in LANDSAT data can be mitigated by applying corrections. We used the radiation transfer physical models (NCEP) developed by Barsi et al. (2003–2005). This includes key variables such as atmospheric transmissivity, and upward and downward radiances. These parameters are an online resource, found at http://atmcorr.gsgc.nasa.gov. Surface emissivity (ε) is defined as the ratio between the target cover emissivity and perfect black body emissivity at the same temperature (Chuvieco, 2007). According to Van de Griend and Owe (1993), and Pasapera-Gonzales (2016), we calculate emissivity by taking into account the existing relationship between the Normalized Difference of Vegetation Index (NDVI) and emissivity (Tucker and Sellers, 1986; Carlson and Ripley, 1997; Rivas and Carmona, 2013). Thus, the corrected superficial radiance based on Barsi et al.'s (2003) eq. (4) can be obtained:

$$Lt = \frac{Ltoa - \tau*(1-\varepsilon)*Ld - Lu}{\tau*\varepsilon} \quad (4)$$

where Lt is corrected superficial radiance; $Ltoa$ corresponds to the radiance received by the sensor; τis atmospheric transmissivity; ε is emissivity; Ld is the downward radiance and Lu is the upward radiance.

2.2.2. IST calculations

The equation used to estimate the surface temperature (T) is an inversion of Planck's equation (Kidwell, 1991), Eq. (5):

$$T\ (^{\circ}C) = \frac{K_2}{Ln\left(1 + \frac{K_1}{Lt}\right)} - 273.39 \quad (5)$$

where $K_2$and $K_1$are known constants (see LANDSAT, 2016), and Lt, the corrected radiance.

2.3. Front fluctuation and calving rate

Corona and Landsat images were used to map the historical reconstruction of the frontal positions from 1979 to 2016. The images were selected according to their availability in the archive. Corona and Hexagon scenes (10 m resolution) (Fowler, 2013) were geometrically treated to eliminate the deformations produced and were geo-referenced through the incorporation of ground control points (GCPs) from Landsat images, and re-sampled to the same spatial resolution as Landsat (Moragues et al., 2018). It is important to notice that an average error of the size of one pixel was found, and this digitizing accuracy is in accordance with the reports by Paul et al. (2013).

On the other hand, the calving rate is an indicator of the changes experienced by the glacier's frontal position. The calving rate is defined as the difference between glacial front flow speed and the length changes during the study period. It can be estimated by means of Eq. (6) (Benn and Evans, 2014):

$$Uc = Uf - \frac{\partial L}{\partial t} \quad (6)$$

where Uc is calving rate, Uf is glacial front flow speed, L is glaciers' length, and t is time.

We calculate the calving rate of each pair considering Uf as the mean surface flow speed of glacier front and L as the difference in front positions between the scenes of each pair (e.g. from October 13 to October 29 and from February 18 to March 21). Thus, $\frac{\partial L}{\partial t}$ is front fluctuation expressed in md^{-1}.

2.4. Ui and IST statistical correlation

Considering that Us obtained by remote sensing for each pair is the mean displacement of the period, in order to obtain the correlation, we calculated the mean IST of the same period. Furthermore, it was necessary to homogenize the spatial resolution of both variables to 100 m. In order to assess and mitigate errors in the correlation between Us and IST, supraglacial debris was identified, as this would alter the surface exposure of the ice and its ice surface temperature. Three testing zones are defined: (A1) Complete cover by supraglacial debris, (A2) supraglacial debris and bared ice facies, (A3) bared ice (Fig. 1). The correlation analysis proposed is based on linear (r_1), quadratic (r_2) and exponential correlation (r_3) (McKillup and Dyar, 2010). We chose a p-value $\leq .0001$ to the analysis that involves minimizing the likelihood that the observed correlations might be random. In our study, correlations were considered valid where the probability that they were random was equal to or $< 0.01\%$.Finally, the testing areas (see Fig. 1) with statistically and glaciological significant results were evaluated by ice creep (Ui) Glen's Flow law to approach to the VG's displacement modes (Section 2.4.1).

2.4.1. Displacement modes

In order to find out the Viedma glacier's displacement modes, it is crucial to understand the processes dominating its dynamics. In this sense, a glacier widely dominated by basal sliding reflects the existence of a large supraglacial, englacial and supraglacial hydrological system. This information is potentially very useful for further research.

Considering that the VG is temperate, Us is defined by Eq. (1); therefore, Us (section 2.1) > Ui. Thus, Us-Ui = Ub. According to Glen's flow law, Ui can be calculated by means of Eq. (7) (Cuffey and Paterson, 2010):

$$U_i = \frac{2A}{n+1}\tau_b{}^n H \quad (7)$$

where A and n are parameters that define the relationship between stress and strain. The flow law exponent n varies but it is usually close to 3 (Benn and Evans, 2014). The rate parameter A increases exponentially with ice temperature (Hooke, 1981). τ_b is shear stress and H is the ice thickness. Thus:

$$A = A_0 \ exp\left[-\frac{Q*}{R_g T_i} + \frac{0.49836}{(T_0 - T_i)^k}\right] \quad (8)$$

where $A_0 = 9.302*10^{-2}\,Pa^{-3}\,yr^{-1}$, Q^* is the activation energy for creep ($7.88*10^4\,J\,mol^{-1}$), R_g is the gas constant ($8.314\,J\,mol^{-1}\,K^{-1}$), T_i is the ice temperature in Kelvins (°K) obtained from LANDSAT images, $T_0 = 273.39$ K and $k = 1.17$. Then τ_b is obtained by Eq. (9) (Benn and Evans, 2014):

$$\tau_b = \rho g H \tan\alpha \quad (9)$$

where ρ is ice density ($850\,kg\,m^{-3}$), g is gravity acceleration and α is the VG's surface slope obtained from the STRM re-sampled to 100 m. In this study, τ_b is calculated with $H = 500$ m considering the bathymetry close to the VG's terminus by Sugiyama et al. (2016) and recent field work (Andrés Rivera, personal communication).

According to Nye (1952), the ice surface profile (H) can be calculated by Eq. (10):

$$H = \sqrt{2h_0 s} \quad (10)$$

where s is the horizontal distance from the margin (in meters) and h_0:

$$h_0 = \frac{\tau_b}{\rho g} \quad (11)$$

3. Results

3.1. Surface Flow Speed (Us)

Many factors affect the accuracy of glacier surface flow speed estimation such as time lapse between images, cloud and snow cover degree and supraglacial geomorphological features (Kääb and Vollmer, 2000; Berthier et al., 2003, 2005; Kumari et al., 2014). Time lapse between images is inversely related to the de-correlations degree. Nevertheless, the 2016 pair has twice the amount of days between images than the 2015 pair but displays very similar amounts of useable data. The explanation lies in the 2015 images being compromised by recent snow. The VG's surface flow speed error analysis shows a Total error of around0.3 md^{-1} and0.04 $md^1$for the 2015 and 2016 pairs respectively, which represents < 10% with respect to the mean velocities detected (Table 2).

The displacement is the highest in the central flow (> 2.4 ± 0.3 md^{-1} and a maximum of around 5.5 ± 0.3 md^{-1} in the 2015 pair) and it decreases toward the glacial margin. Another aspect to be highlighted which is observed in Fig. 3 corresponds to the VG's terminus flow speed increase. Maximum velocities of around 3 md^{-1} were observed at calving front for both pairs. This could be explained by the reduction in basal drag, which can be greatly affected by the presence of water at the glacier margin, especially if it is deep enough for the ice to float fully or partially (Benn and Evans, 2014; Post et al., 2011). Also, we detected a flow direction change at the VG's terminus between the 2015 and 2016 pair. The lost mass at terminus by calving and its front retreat beyond the curve may explain this change (Fig. 3).

Another site that showed flow speed acceleration is the VG's margin adjacent to the Viedma lagoon, located at the southern margin of the homonymous glacier (see Fig. 3). It is an ice-dammed lagoon produced by melt water from alpine glaciers located upstream and retained by the VG's southern margin. This zone reached surface flow speeds of 1.3 md^{-1}, which were significant in comparison with a margin speed of around 0.6 md^{-1} or less. Such acceleration could be the result of a similar process occurring at VG's terminus. Ice-dammed lakes or lagoons frequently exhibit level fluctuation due to the drainage of adjacent glaciers (Tweed and Russell, 1999). Therefore, the movement of the VG would alter the lagoon drainage with consequent glacier velocity changes by melt water supply and effective pressure decrease.

Comparatively, results reveal that the 2016 pair showed higher surface velocities than the 2015 pair, and this trend is exposed in transverse and axial profiles P1, P2 and P3 (see Fig. 3) and Fig. 4a. These differences could be explained by the greater availability of melt water and better development of the englacial and subglacial drainage networks toward the mid and end warm season with respect to the beginning of the same season (Fig. 4b, c, d) (Iken and Bindschadler, 1986; Sugiyama et al., 2011; Vincent and Moreau, 2016).

Table 2
Final quantity of reliable data. In all cases, the absolute values represent the amount of data available after applying the respective filters. The final post-filter proportion of data is also given.

	2015 pair	%	2016 pair	%
Δt [days]	16		32	
Available records after CIAS	509,071	100	506,226	100
Available records after filtering by maximum correlation (≥0.7)	191,477	38	192,855	38
Available records after Directional filter	185,746	36	192,325	38

3.2. Ice Surface Temperatures (IST)

IST results revealed two patterns of spatial distribution. One of them is a thermal gradient transversal to the flow which decreases from the margins of the glacier, in contact with the rock, toward the center, until it comes in contact with several central moraines, where, again, a thermal increase occurs (Fig. 5). Fig. 5 links thermal variability along profile P2 (2016 pair) with different covers on the surface. The profile suggests that the greater the amount of supraglacial debris, the higher the temperature observed. On the other hand, the zones with bared ice reported the lowest temperatures throughout the whole sequence, without exception. The second thermal patterns showed a gradient inversely related to the altitude variations. Thus, the VG's terminus showed the highest surface temperatures (Fig. 6). Another process that turns the glacier front into a warm zone is its interaction with the Viedma lake, which entails a transfer of heat from water to ice. According to Sugiyama et al. (2016) the top layer of the Viedma lake is warm and reaches temperatures above 6 °C.

On the other hand, in both pairs (2015 and 2016), the IST values on the ice are, in many cases, higher than 0 °C. The signal captured by the 100 m pixel integrates the ice signal along with supraglacial debris and supraglacial melt water. Comparatively, 82% of the time, the 2016 pixel-to-pixel temperatures were higher than in 2015. The widespread IST above pressure melting point reflects the supraglacial melt water runoff. This may occur due to the greater insolation received by the glacier in February–March compared to October (southern hemisphere).

3.3. Front fluctuation and calving rate

Considering the front mean Us (2015 = 2.6 md^{-1} and 2016 = 2.5 md^{-1}) and the maximum difference of front position changes (2015 = −146 m/16d = −9.1 md^{-1} and 2016 = −164 m/32d = −5.1 md^{-1}), mean calving rates for both pairs were calculated. In 2015, the calving rate was equal to 11.7 $md^{-1}$and, in the 2016 pair, it was equal to 7.6 md^{-1}. Taking into account that, in both periods, the surface mean velocities were similar, it was the changes in front positions which determined the difference in the calving rate.

According to our reconstruction of front fluctuation, the VG

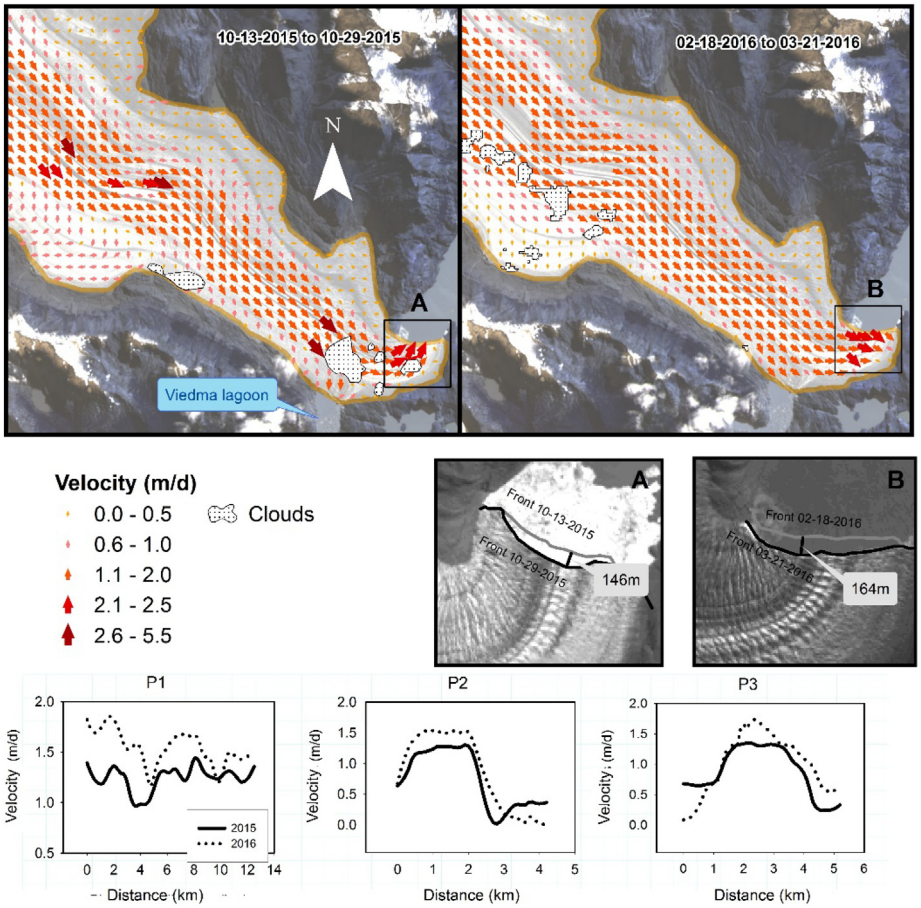

Fig. 3. Viedma glacier's surface flow speed for the2015 and 2016 pairs. A) Front fluctuation for the 2015 pair. B) Front fluctuation for the 2016 pair. Bottom: P1, P2 and P3 are surface velocity profiles (see Fig. 1).

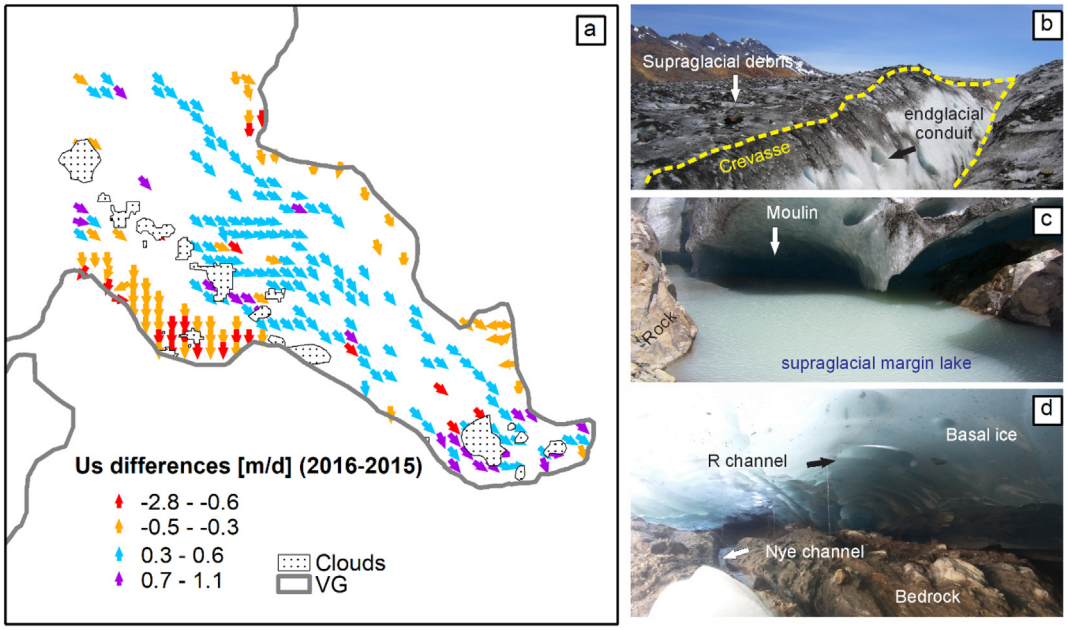

Fig. 4. a) Us difference between the 2016 and 2015 pairs. Positive values denote higher Us for the 2016 pair than for the 2015 pair. Only Us differences higher than the Total error = 0.3 md^{-1} were mapped. b) Supraglacial debris and englacial conduits are being showed. It is common for crevasses to act as vertical conduits between surface and glacier bed. c) Marginal water supply to glacier bed through moulins. d) Glacier bed and bedrock denote the melt water flow.

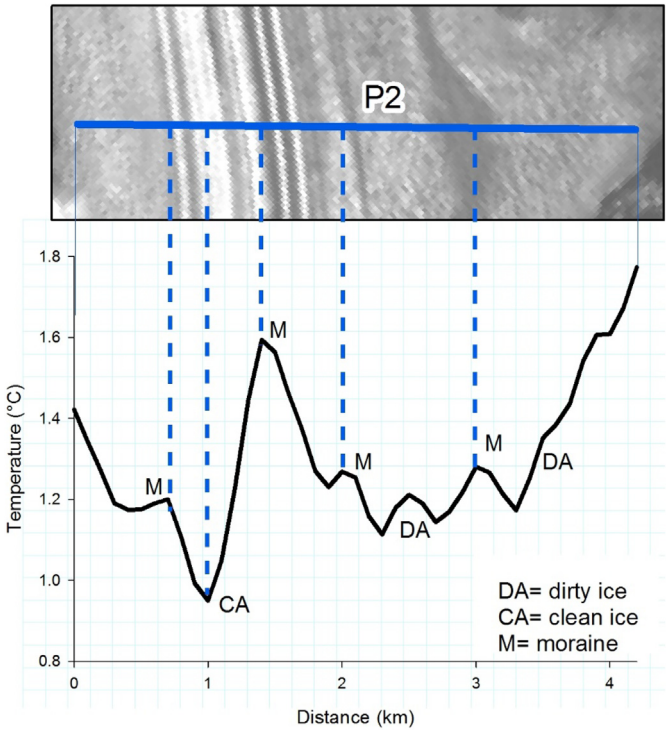

Fig. 5. IST profile (P2–2016 pair). The figure shows the IST distribution on a transversal profile and its change in relation to the different covers present at the VG's surface.

receded > 3.5 km from 1976 to May 2016 (40 years), with a mean rate of 87.5 my^{-1} (see Fig. 7). Over the last 12 years (2005–2016) the VG receded by 50% of the total retreat observed in the series, reaching a mean rate of 155 my^{-1}. In particular, the 2010–2016 period showed an abrupt acceleration of frontal retraction, with a mean rate equal to 281 my^{-1} and an intensification as from 2015. This constitutes the highest retraction rate observed, at least, over the last 40 years on the VG.

3.4. Us and IST statistical correlation analysis

3.4.1. Testing areas

Correlation analysis between surface flow speed and surface temperatures was applied to each testing area (see Fig. 1) of the 2015 and 2016 pairs, obtaining 6 correlation pairs (A1–15, A2–15, A3–15, A1–16, A2–16, A3–16). A first statistical approximation shows that only the bared ice test area (A3) had statistical significance and coherence with respect to the correlation (+) and in its coefficients between the 2015 pair (r = 0.49) and the 2016 pair (r = 0.48) (Fig. 8). This situation is in line with Glen's flow law (Paterson, 1969; Benn and Evans, 2014; Cuffey and Paterson, 2010), who defines positive relations between ice temperatures and displacements by deformation or ice creep. Conversely, the test zones with total (A1) and partial (A2) coverage of the ice by supraglacial debris showed inconsistencies when comparing the same area in the two periods. In particular, the A1–15 and A2–15 were not statistically significant, while those from the 2016 pair met this condition. According to the correlation coefficient, the correlation sense of A1–16 and A2–16 was negative. However, the graphical analysis shows the absolute independence of the two variables without a definite sense. This reflects the distortion generated by the presence of supraglacial debris in the correlation and the importance of eliminating this influence on analysis.

3.4.2. Displacement modes

Considering that A3 was the only zone with statistically and glaciologically significant results, displacement analysis by ice deformation (Ui) was applied to it. First, we estimated Ui on area A3 according to Eq. 6. Secondly, we compared Ui with Us results, which approached us to Ub. Considering that the A parameter (Eq. 7) only applies to IST ≤ 0 °C or 273.39 °K, thus, Ui was calculated only on the 2015 pair.

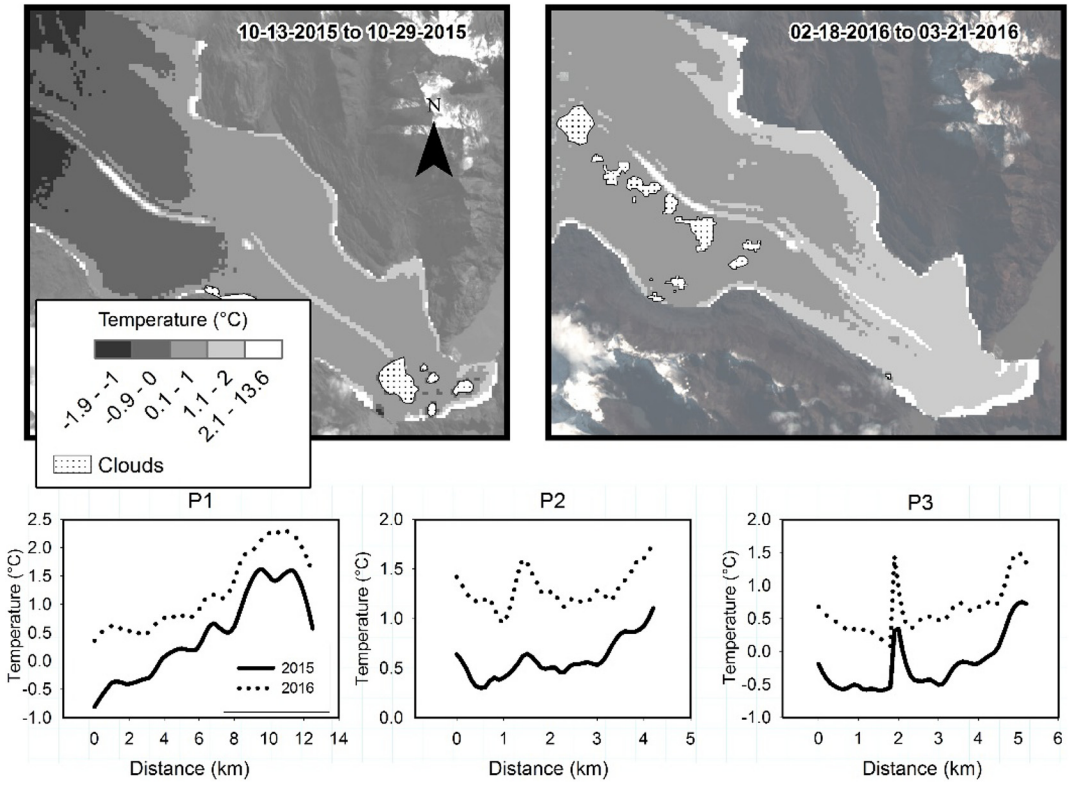

Fig. 6. IST spatial distribution at the Viedma glacier in the 2015 and 2016 pairs. P1, P2 and P3 correspond to the IST profiles shown in Fig. 1.

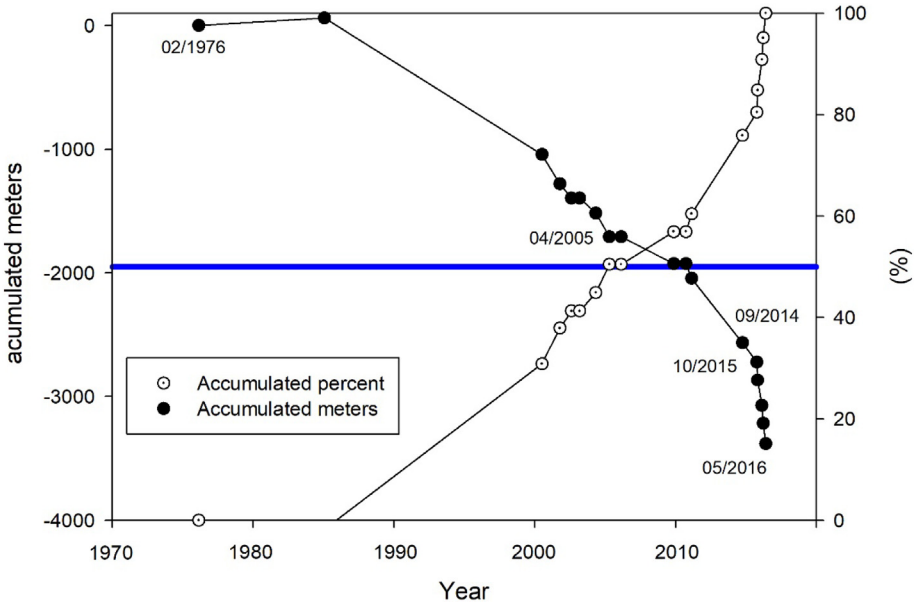

Fig. 7. Accumulated VG front evolution from February 1976 to May 2016. The negative tendency indicates the front retraction from its position in February 1976. The primary Y axis shows the accumulated front fluctuations on absolute value (m), while the secondary Y axis does the same in relative terms (%). History reconstructed from CORONA and LANDSAT imagery. The blue line marks the 50% of total retraction. (For interpretation of the references to colour in this figure legend, the reader is referred to the web version of this article.)

Results suggest that A3 was widely dominated by Ub, which was over a 90% of Us. Fig. 9a and 9b show the relationship between the A parameter and Ui, and between the A parameter and Us. In this sense, Fig. 9a shows the dependence of Ui with respect to A, whereas 9b shows a more diffuse relationship between Us and A. This reinforces the idea that VG A3 was dominated by basal sliding (Fig. 9c). Besides, Fig. 9c shows the importance of slope in Ui displacement, for example, to 4800 m from terminus. This matches our field observation with respect to the VG's wavy surface.

Thus, our hypothesis proposes that, in the warm season, displacements by basal sliding are predominant in relation to deformation displacements due to the highest availability of supraglacial, englacial and subglacial runoff.

4. Discussion

4.1. Surface flow speed

The SPI glaciers are some of the fastest moving in the world, except for various cases observed in Greenland (Mouginot and Rignot, 2015). Example of that are the Penguin (28 md^{-1}), Europa (24 md^{-1}), HPS-19 (16 md^{-1}) and Upsala glaciers (6.6 md^{-1}). They are, respectively, 5, 4, 3 and 1.2 times faster than the maximum surface flow speed registered in our study (5.5 md^{-1}).

According to Sakakibara and Sugiyama (2014), the VG experienced surface flow speed changes between 1984 and 2011. In particular, the 1984–2000 period was defined by an increase of around 3%, whereas the 2000–2011 period showed a decrease of 5.3%.However, the relative decrease of surface flow speed was not accompanied by a front retreat decrease. Riveros et al. (2013) and Euillades et al. (2016) estimated surface velocities (2012 cold season, and 2012 cold and warm seasons, respectively) by means of SAR techniques and reported Us of around 3 md^{-1}in front area and of 2 md^{-1} in central flow of middle basin. Besides, Lenzano et al. (2018),from time-lapse daily optical images, by using terrestrial cameras, found surface mean velocities of 3.5 ± 0.36 md^{-1} at the VG's terminus (from April 2014 to April 2016). Euillades et al. (2016) suggested that these high surface flow speeds appear to be governed by the decrease in effective pressure associated with the glacier incoming into the lake. The comparison of our results with other preceding studies showed a high correspondence. The different values of velocities found in such investigations may be explained by the different sensors, geospatial data acquisition platforms and techniques used (Lenzano et al., 2018) and due to the fact that the studies were carried out on different periods.

4.2. Ice surface temperature

The present study is the first one to report IST values from the Viedma glacier and the SPI. Therefore, we cannot contrast our results with other IST values in the same area. However, IST studies have been conducted in other parts of the world such as the Himalaya, China and Greenland (Hall et al., 2008; Raj and Fleming, 2008; Hall et al., 2012; Haq et al., 2012; Hall et al., 2013; Wu et al., 2015). As our results, they showed IST values above pressure melt point in the warm season and suggested the supraglacial melt water presence. In this regard, Hall et al. (2013) recovered Greenland's melt areas from IST values.

Furthermore, they highlighted that IST is one of the most important parameters for estimating the effect of climatic change on glaciers. Unfortunately, estimating surface temperature by using traditional weather-station based meteorological observations is not a feasible solution as they will not be representative of all three Snout, ELA and Max. glacier altitudes. Therefore, through remote sensing studies, a synoptic view of different regions can be established and used for regional climatological studies (Raj and Fleming, 2008).

4.3. Front fluctuation and calving rate

According to López et al. (2010), the VG retreated < 1 km during the 1945–2005 period, a distance representing 0.4% of the glacier's length in 1945, (63.1 km). Then, Sakakibara and Sugiyama (2014) reported that the VG's front retreated to mean rates of 35.5 my^{-1} from 1984 to 2011. During this period, the VG changed little in contrast with Upsala (272 my^{-1}), Jorge Mont (390 my^{-1}) and HPS-12 (334 my^{-1}). However, our results showed that, during the 2010–2016 period, the VG's front retreat increased drastically, to a mean retreat rate of 281 my^{-1}.This rate is comparable with those of the Upsala (270 my^{-1}) and Jorge Mont (240 my^{-1}) glaciers during the 2000–2011 period, which are considered to have the greatest retreat rate among the SPI glaciers (Sakakibara and Sugiyama, 2014).

Taking into account that a) in the 2015 pair, the calving rate was equal to 11.7 md-1and, in the 2016 pair, it was equal to 7.6 md-1, and that b) in both periods, the surface mean velocities were similar, it was the front position changes which determined the difference in the calving rate. At this point, it is necessary to mention the lake bed

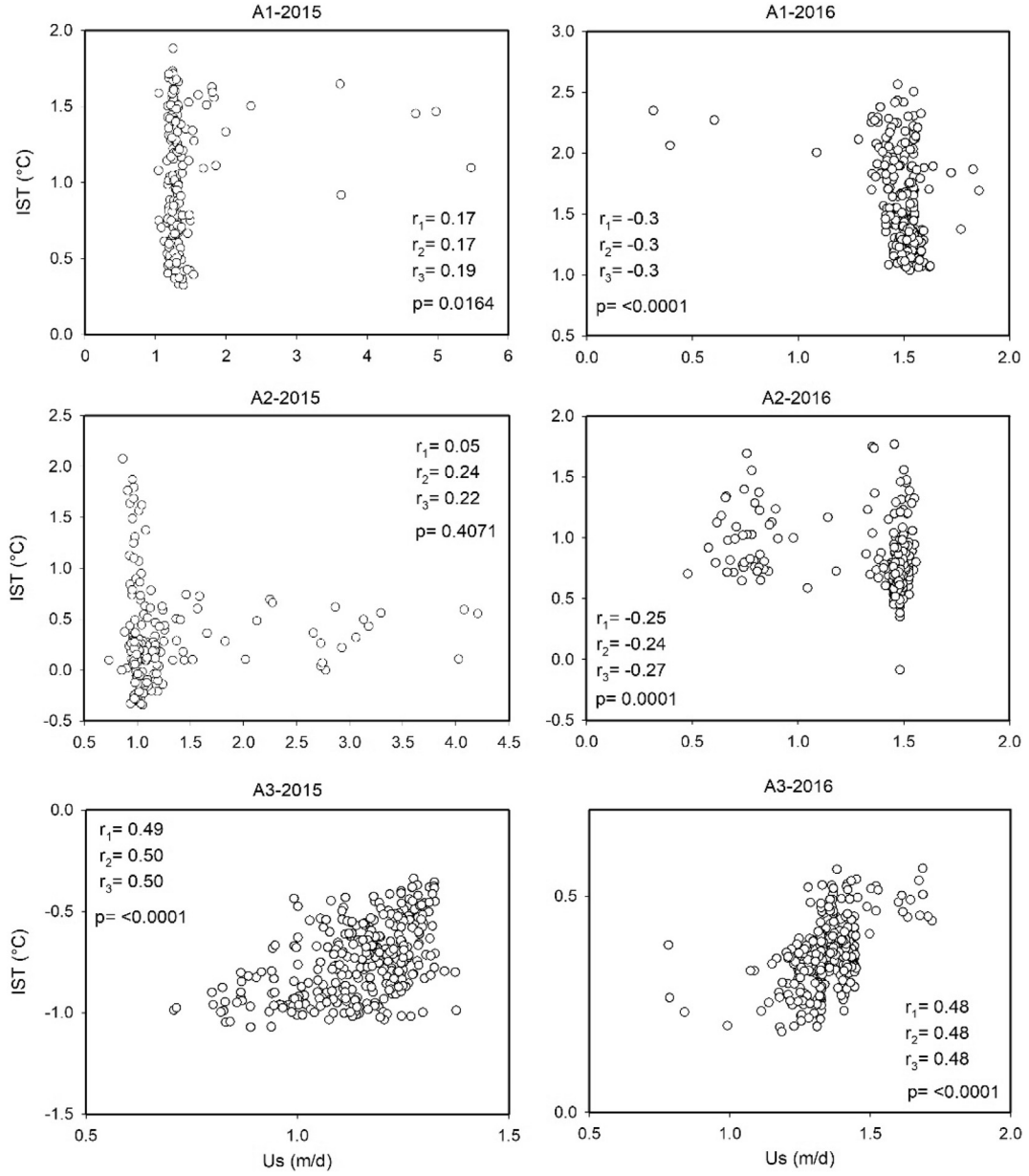

Fig. 8. Scatter plots between Us and IST to each testing area (A1, A2 and A3) and pair (2015 and 2016). Where A1 corresponds to the sampling performed on sectors completely covered with supraglacial debris, A2 to a mixture between covered and bared ice, and A3 to zones with bared ice (Fig. 1).r_1 is linear correlation coefficient, r_2 is quadratic correlation coefficient and r_3 is exponential correlation coefficient.

morphometry immediately below the glacial front in each analysis pair (Warren et al., 1995; Post et al., 2011). In this sense, Sugiyama et al. (2016) showed maximum depths of around 400 m close to the VG's front at the Viedma lake. Recently, surveyed bathymetry of the Viedma lake reported water depths of up to 571 m close to the VG's front (Andrés Rivera, personal communication)

4.4. Displacement modes

Changes in basal water pressure play a critical role in short-term ice speed variations; it is controlled primarily by the melt water production rate (Sugiyama et al., 2016). Ub has been measured on some glaciers in subglacial cavities and tunnels or by drilling boreholes down to the glacier bed. These observations support an interpretation of the sliding mechanism as a jerky movement (Stuefer, 1999).

Our results suggested that A3 is governed by Ub. Although no Ub measurements have been carried out on the Viedma glacier, Stuefer (1999) on the Perito Moreno glacier showed that Ub represented over a 90% of Us, at least from 5 km from the terminus. According to Mouginot and Rignot (2015), if an ice thickness of around 700 m is assumed on the SPI plateau, the ice flow from internal deformation (Ui) of temperate ice should be less than about 50 myr^{-1} (or 0.13 md^{-1}), which indicates that large portions of the icefields must be sliding over their beds. This is contrary to the traditional view that internal deformation dominates the flow in the interior regions and fast sliding only dominates along the periphery. In Patagonia, it has been observed that the vast majority of the icefields must be influenced by sliding (Mouginot and Rignot, 2015).

Finally, despite the fact that it is more common to use the A parameter as a constant, the importance of estimating the A parameter on each site of the glacier is a point for discussion. Note that Stuefer (1999) showed that changing the A parameter for the same place, the UI estimation may change more than ± 1 md^{-1}.In this sense, IST by remote sensing turns out to be a good way to make up for the lack of data.

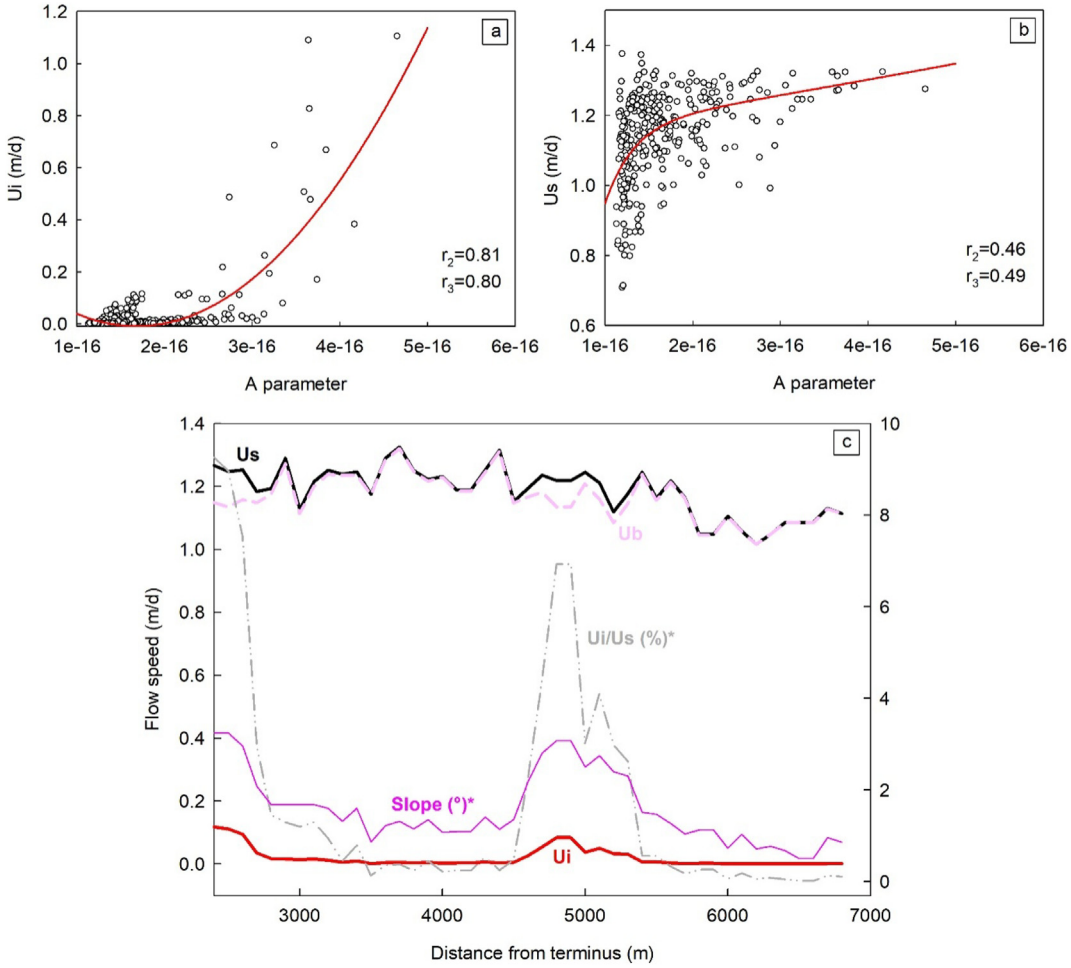

Fig. 9. a) shows the scatterplot between the A parameter and Ui for the 2015 pair. b) shows the scatterplot between the A parameter and Us for the 2015 pair. r2 is quadratic correlation coefficient and r_3 is exponential correlation coefficient. c) VG displacement modes for the A3–2015 testing area. Variables labeled with * are showed at secondary axis Y (right).

5. Conclusions

It is important to highlight the high capacities of the LANDSAT multispectral sensor in monitoring different physical aspects of the glaciers with recordings captured on the same day, same hour and same angle of vision but in different wavelengths. The spatial, spectral and temporal performance of remote sensing data enables the accurate modeling of the Viedma glacier's physics and its dynamics.

From the results obtained, it can be concluded that the tracking feature is a robust technique in terms of the correlation algorithm and for obtaining accurate velocity fields. In this sense, the calculated uncertainties are acceptable with respect to the magnitude of the speeds that characterize the glacier under study (< 10% of the mean velocities value). The difficulty of having images with a clear and bared atmosphere in areas such as the Southern Patagonian Ice Field becomes a limitation when using satellite images as input data.

Regarding the surface flow speed values, the most important one is the flow acceleration (3 md^{-1}) at the Viedma glacier's terminus, due to the calving process, which is similar to that observed on the Viedma glacier's southern margin in contact with the Viedma lagoon. Also, in the year 2015, the Viedma glacier showed the highest recoil rates over the last 40 years.

On the other hand, IST estimation yielded results that confirmed the good abilities and capacities of thermal bands as a starting point for future studies related to glacial dynamics and its behavior. It is important to mention the possibility of including atmospheric and emissivity corrections as key elements in order to obtain good results. Note that a thermal band value with a spatial resolution equal to 100 m in many cases showed a combination of covers with different temperatures such as bared ice, supraglacial debris and melt water.

From the point of view of statistical analysis, the results obtained are promising with a view to studying the correlation between velocities and surface temperatures. At this point, it is important to reiterate the need of contemplating the diversity of covers present on glacial surface when searching for such relationships; the omission of this aspect could lead to biased results.

Finally, our results suggest that, at least, the middle and low basins of the Viedma glacier are governed by basal sliding. These results are the first approach to the study of displacement modes by remote sensing in this area, and they constitute a promising basis to improving understanding of the SPI glaciers' dynamics. This idea is reinforced by the lack of previous field measurements and the environmental difficulties presented for exploration of the entire SPI.

Acknowledgments

We want to thank Los Glaciares National Park, especially park rangers Jorge Lenz and Alejandro Caparrós. The study was supported by grant PICT 1995-2013, Agencia Nacional de Ciencia y Tecnología Argentina (ANCyT). Finally, we want to thank Adalberto Ferlito and Daniel Falaschi for their help in the work field.

References

Aniya, M., Skvarca, P., 1992. Characteristic and variations of Upsala and Moreno glaciers, Southern Patagonia. Bulletin of glacier Research 10, 39–54.

Aniya, M., Sato, H., Naruse, R., Skvarca, P., Casassa, G., 1996. The use of Satellite and Airborne Imagery to Inventory Outlet Glaciers of the Southern Patagonia Icefield, South America. Photogramm. Eng. Remote Sens. 62 (12), 1361–1369.

Arendt, et al., 2012. RGI Version 2.0: released June 12, 2012. In: Version 2.0 includes metadata on data sources, outlining techniques and incorporates newly available outlines, link. http://www.glims.org/RGI/RGI_Tech_Report_V2.0.pdf.

Barsi, J.A., Barker, J.L., Schott, J.R., 2003. An atmospheric correction parameter calculator for a single thermal band earth-sensing instrument. In: Geoscience and Remote Sensing Symposium, 2003. IGARSS'03. Proceedings. 2003 IEEE International Vol. 5. IEEE, pp. 3014–3016.

Barsi, J.A., Schott, J.R., Palluconi, F.D., Hook, S.J., 2005. Validation of a web-based atmospheric correction tool for single thermal band instruments. In: Optics & Photonics 2005. International Society for Optics and Photonics.

Benn, D., Evans, D., 2014. Glaciers & glaciation. Routledge publishing, New York, USA.

Bennett, M.M., Glasser, N.F. (Eds.), 2011. Glacial geology: Ice sheets and landforms. John Wiley & Sons..

Berthier, E., Raup, B., Scambos, T., 2003. New velocity map and mass-balance estimate of Mertz Glacier, East Antarctica, derived from Landsat sequential imagery. J. Glaciol. 49 (167), 503–511.

Berthier, E., Vadon, H., Baratoux, D., Arnaud, Y., Vincent, C., Feigl, K.L., Legresy, B., 2005. Surface motion of mountain glaciers derived from satellite optical imagery. Remote Sens. Environ. 95 (1), 14–28.

Berthier, E., Cabot, V., Vincent, C., Six, D., 2016. Decadal Region-Wide and Glacier-Wide Mass Balances Derived from Multi-Temporal ASTER Satellite Digital Elevation Models. Validation over the Mont-Blanc Area. Frontiers of Earth Science 4, 63. https://doi.org/10.3389/feart.2016.00063.

Bown, F., Rivera, A., Acuña, C., 2008. Recent glacier variations at the Aconcagua basin, central Chilean Andes. Ann. Glaciol. 48 (1), 43–48.

Carlson, T.N., Ripley, D.A., 1997. On the relation between NDVI, fractional vegetation cover, and leaf area index. Remote Sens. Environ. 62 (3), 241–252.

Chen, J.L., Wilson, C.R., Tapley, B.D., Blankenship, D.D., Ivins, E.R., 2007. Patagonia icefield melting observed by gravity recovery and climate experiment (GRACE). Geophys. Res. Lett. 34 (22).

Chuvieco, E., 2007. Teledetección Ambiental. La observación de la Tierra desde el espacio. Ariel, Barcelona.

Cuffey, K.M., Paterson, W.S.B., 2010. The physics of glaciers. Academic Press.

Davies, B.J., Glasser, N.F., 2012. Accelerating shrinkage of Patagonian glaciers from the Little Ice Age (~ AD 1870) to 2011. J. Glaciol. 58 (212), 1063–1084.

Euillades, L.D., Euillades, P.A., Riveros, N.C., Masiokas, M.H., Ruiz, L., Pitte, P., ... Balbarani, S., 2016. Detection of glaciers displacement time-series using SAR. Remote Sens. Environ. 184, 188–198.

Fowler, M.J.F., 2013. Declassified Intelligence Satellite Photographs. In: Hanson, W.S., Oltean, I.A. (Eds.), Archaeology from historical aerial and satellite archives. Springer Science, Business Media, Berlin, pp. 47–66.

Garreaud, R.D., 2009. The Andes climate and weather. Adv. Geosci. 22, 3.

Garreaud, R.D., Gabriela Nicora, M., Bürgesser, R.E., Ávila, E.E., 2014. Lightning in western Patagonia. Journal of Geophysical Research: Atmospheres 119 (8), 4471–4485.

Hall, D.K., Box, J.E., Casey, K.A., Hook, S.J., Shuman, C.A., Steffen, K., 2008. Comparison of satellite-derived and in-situ observations of ice and snow surface temperatures over Greenland. Remote Sens. Environ. 112 (10), 3739–3749.

Hall, D.K., Comiso, J.C., Di Girolamo, N.E., Shuman, C.A., Key, J.R., Koenig, L.S., 2012. A satellite-derived climate-quality data record of the clear-sky surface temperature of the Greenland ice sheet. J. Clim. 25 (14), 4785–4798.

Hall, D.K., Comiso, J.C., Di Girolamo, N.E., Shuman, C.A., Box, J.E., Koenig, L.S., 2013. Variability in the surface temperature and melt extent of the Greenland ice sheet from MODIS. Geophys. Res. Lett. 40 (10), 2114–2120.

Haq, M.A., Jain, K., Menon, K.P.R., 2012. Surface temperature estimation of Gangotri Glacier using thermal remote sensing. ASTER 47, 15–87.

Heid, T., Kääb, A., 2012. Evaluation of existing image matching methods for deriving glacier surface displacements globally from optical satellite imagery. Remote Sens. Environ. 118, 339–355.

Herman, F., Anderson, B., Leprince, S., 2011. Mountain glacier velocity variation during a retreat/advance cycle quantified using sub-pixel analysis of ASTER images. J. Glaciol. 57 (202), 197–207.

Hooke, R.L., 1981. Flow law for polycrystalline ice in glaciers comparison of theoretical predictions, laboratory data, and field. Rev. Geophys. Space Phys. 19 (4), 664–672.

Iken, A., Bindschadler, R.A., 1986. Combined measurements of subglacial water pressure and surface velocity of Findelengletscher, Switzerland: conclusions about drainage system and sliding mechanism. J. Glaciol. 32 (110), 101–119.

Ivins, E.R., Watkins, M.M., Yuan, D.N., Dietrich, R., Casassa, G., Rülke, A., 2011. On-land ice loss and glacial isostatic adjustment at the Drake Passage: 2003–2009. Journal of Geophysical Research: Solid Earth 116 (B2).

Jaber, W.A., Floricioiu, D., Rott, H., Eineder, M., 2012. Dynamics of fast glaciers in the Patagonia Icefields derived from Terrasar-X and Tandem-X data. In: 2012 IEEE, International Geoscience and Remote Sensing Symposium. IEEE, pp. 3226–3229.

Kääb, A., Leprince, S., 2014. Motion detection using near-simultaneous satellite acquisitions. Remote Sens. Environ. 154, 164–179.

Kääb, A., Vollmer, M., 2000. Surface geometry, thickness changes and flow fields on creeping mountain permafrost: automatic extraction by digital image analysis. Permafr. Periglac. Process. 11, 315–326.

Kidwell, K., 1991. NOAA polar orbiter data user's guide. Washington D.C, National Climatic Data Centre.

Kumari, S., Ghosh, S.K., Buchroithner, M.F., 2014. Measurement of glacier velocity at Pik Lenin, Tajikistan, by feature tracking. In: The International Archives of Photogrammetry, Remote Sensing and Spatial Information Sciences. 40(8). pp. 531.

LANDSAT, 2016. LANDSAT Missions. United State Geological Survey (USGS). http://landsat.usgs.gov//landsat_level_1_standard_data_products.php.

Lenzano, M.G., Lannutti, E., Toth, C., Rivera, A., Lenzano, L., 2018. Time-lapse series and optical flow implementation in Viedma glacier to derive surface motion during 2014–2016 period. PE&RS.

Liboutry, L., 1956. Nieves y glaciares: fundamentos de glaciología. Ediciones Universidad de Chile, Santiago 471p.

Lopez, P., Chevallier, P., Favier, V., Pouyaud, B., Ordenes, F., Oerlemans, J., 2010. A regional view of fluctuations in glacier length in southern South America. Glob. Planet. Chang. 71 (1), 85–108.

Meikle, H., 2008. Modern Radar System, Second edition. Artech house, London.

Möller, M., Schneider, C., Kilian, R., 2007. Glacier change and climate forcing in recent decades at Gran Campo Nevado, southernmost Patagonia. Ann. Glaciol. 46 (1), 136–144.

Moragues, S., Lenzano, M.G., Lo Vecchio, A., Falaschi, D., Lenzano, L., 2018. Surface velocities of glaciar Upsala, Southern Patagonian Andes, using cross correlation of ASTER satellite images. Andean Geol. 45, 87–103.

Mouginot, J., Rignot, E., 2015. Ice motion of the Patagonian icefields of South America: 1984–2014. Geophys. Res. Lett. 42 (5), 1441–1449.

Naruse, R., Aniya, M., 1992. Outline of Glacier Research Projecting Patagonia, 1990. Bulleting of Glacier Research 10, 31–38.

NASA, 2017. Landsat Science. Obtained of. https://landsat.gsfc.nasa.gov/wp-content/uploads/2016/08/Landsat7_Handbook.pdf.

Nye, J.F., 1952. A method of calculating the thickness of ice sheets. Nature 169, 529–530.

Pasapera-Gonzales, J.J., 2016. Validación de la Emisividad y Temperatura de la Superficie del suelo usando datos del satélite Landsat 8. Universidad de Córdoba, Argentina, pp. 223.

Paterson, W. S. B.1969. The Physics of Glaciers. *Pergamon Press Ltd. General editors: J.A. Jacobs and J.T. Wilson.*

Paul, F., Barrand, N.E., Baumann, S., Berthier, E., Bolch, T., Casey, K., Mölg, N., 2013. On the accuracy of glacier outlines derived from remote-sensing data. Ann. Glaciol. 54 (63), 171–182.

Pfeffer, W.T., Arendt, A.A., Bliss, A., Bolch, T., Cogley, J.G., Gardner, A.S., ... Miles, E.S., 2014. The Randolph Glacier Inventory: a globally complete inventory of glaciers. J. Glaciol. 60 (221), 537–552.

Post, A., O'Neel, S., Motyka, R.J., Streveler, G., 2011. A complex relationship between calving glaciers and climate. Eos, Transactions American Geophysical Union 92 (37), 305–306.

Raj, K.B.G., Fleming, K., 2008. Surface temperature estimation from Landsat ETM + data for a part of the Baspa basin, NW Himalaya-India. Bull. Glaciol. Res. 25, 19–26.

Rivas, R.E., Carmona, F., 2013. Evapotranspiration in the Pampean Region using field measurements and satellite data. Physics and Chemistry of the Earth, Parts A/B/C 55, 27–34.

Rivera, A., Corripio, J.G., Brock, B., Clavero, J., Wendt, J., 2008. Monitoring ice-capped active Volcán Villarrica, southern Chile, using terrestrial photography combined with automatic weather stations and global positioning systems. J. Glaciol. 54 (188), 920–930. https://doi.org/10.3189/002214308787780076.

Rivera, A., Corripio, J., Bravo, C., Cisternas, S., 2012. Glaciar Jorge Mont (Chilean Patagonia) dynamics derived from photos obtained by fixed cameras and satellite image feature tracking. Ann. Glaciol. 53 (60), 147–155.

Riveros, N., Euillades, L., Euillades, P., Moreiras, S., Balbarani, S., 2013. Offset tracking procedure applied to high resolution SAR data on Viedma Glacier, Patagonian Andes, Argentina. Adv. Geosci. 35, 7–13.

Sakakibara, D., Sugiyama, S., 2014. Ice-front variations and speed changes of calving glaciers in the Southern Patagonia Icefield from 1984 to 2011. Journal of Geophysical Research: Earth Surface 119 (11), 2541–2554.

Scambos, T.A., Dutkiewicz, M.J., Wilson, J.C., Bindschadler, R.A., 1992. Application of image cross-correlation to the measurement of glacier velocity using satellite image data. Remote Sens. Environ. 42 (3), 177–186.

Scherler, D., Leprince, S., Strecker, M.R., 2008. Glacier-surface velocities in alpine terrain from optical satellite imagery—Accuracy improvement and quality assessment. Remote Sens. Environ. 112 (10), 3806–3819.

Shukla, A., Arora, M.K., Gupta, R.P., 2010. Synergistic approach for mapping debris-covered glaciers using optical–thermal remote sensing data with inputs from geomorphometric parameters. Remote Sens. Environ. 114 (7), 1378–1387.

Skvarca, P., De Angelis, H., Naruse, R., Warren, C., Aniya, M., 2002. Calving rates in fresh water: new data from southern Patagonia. Ann. Glaciol. 34, 379–384.

Solomina, O.N., Bradley, R.S., Joelle, V., Geirsdottir, A., Kaufman, D.S., Koch, J., ... Nicolussi, K., 2016. Glacier fluctuations during the past 2000 years. Quat. Sci. Rev. 149, 61–90.

Stern, C.R., Futa, K., Muehlenbachs, K., 1984. Isotope and trace element data for orogenic andesites from the Austral Andes, Andean Magmatism—Chemical and Isotopic Constraints. RS Harmon, BA Barreiro, pp. 31–46.

Stuefer, M., 1999. Investigations on mass balance and dynamics of moreno glacier based on field measurements and satellite imagery. PhD Thesis In: Dissertation zurErlangung des akademischen Grades einesDoktors der Naturwissenschaftenan der Leopold-Franzens-Universitat Innsbruck, 163 pp.

Stuefer, M., Rott, H., Skvarca, P., 2007. Glaciar Perito Moreno, Patagonia: climate sensitivities and glacier characteristics preceding the 2003/04 and 2005/06 damming events. J. Glaciol. 53 (180), 3–16.

Sugiyama, S., Skvarca, P., Naito, N., Enomoto, H., Tsutaki, S., Tone, K., ... Aniya, M.,

2011. Ice speed of a calving glacier modulated by small fluctuations in basal water pressure. Nat. Geosci. 4 (9), 597–600.
Sugiyama, S., Minowa, M., Sakakibara, D., Skvarca, P., Sawagaki, T., Ohashi, Y., Naito, N., Chikita, K., 2016. Thermal structure of proglacial lakes in Patagonia. Journal of Geophysical Research: Earth Surface 121, 2270–2286. https://doi.org/10.1002/2016JF004084.
Tucker, C.J., Sellers, P.J., 1986. Satellite remote sensing of primary production. Int. J. Remote Sens. 7 (11), 1395–1416.
Tweed, F.S., Russell, A.J., 1999. Controls on the formation and sudden drainage of glacier-impounded lakes: implications for jökulhlaup characteristics. Prog. Phys. Geogr. 23 (1), 79–110.
Van de Griend, A.A., Owe, M., 1993. On the relationship between thermal emissivity and the normalized difference vegetation index for natural surfaces. Int. J. Remote Sens. 14 (6), 1119–1131.
Vincent, C., Moreau, L., 2016. Sliding velocity fluctuations and subglacial hydrology over the last two decades on Argentière glacier. Mont Blanc area. *Journal of Glaciology* 1–11.
Warren, C.R., Greene, D.R., Glasser, N.F., 1995. Glaciar Upsala, Patagonia: rapid calving retreat in fresh water. Ann. Glaciol. 21 (1), 311–316.
Whillans, I.M., Tseng, Y.H., 1995. Automatic tracking of crevasses on satellite images. Cold Reg. Sci. Technol. 23 (2), 201–214.
Willis, I.C., 1995. Intra-annual variations in glacier motion: a review. Prog. Phys. Geogr. 19, 61–106.
Willis, M.J., Melkonian, A.K., Pritchard, M.E., Rivera, A., 2012. Ice loss from the Southern Patagonian Ice Field, South America, between 2000 and 2012. Geophys. Res. Lett. 39 (17).
Wu, Y., Wang, N., He, J., Jiang, X., 2015. Estimating mountain glacier surface temperatures from Landsat-ETM+ thermal infrared data: A case study of Qiyi glacier, China. Remote Sens. Environ. 163, 286–295.